Earth Planet. Sci. Lett. 692 (2026) 120246

Contents lists available at ScienceDirect

Earth and Planetary Science Letters

journal homepage: www.elsevier.com/locate/epsl

Experimental evidence for metallic melt trapping in the deep Martian mantle – Implications for inefficient melt segregation and highly siderophile element retention

Kyusei Tsuno [a,b,*], Hideharu Kuwahara [c], Varun Manilal [a], Axel Wittmann [b], Kurt Leinenweber [b,d], Tetsuo Irifune [c], Damanveer S Grewal [a,*]

[a] Department of Earth and Planetary Sciences, Yale University, New Haven, CT, 06511, United States
[b] Eyring Materials Center, Arizona State University, Tempe, AZ, 85287, United States
[c] Geodynamic Research Center, Ehime University, Matsuyama, 790-8577, Japan
[d] School of Molecular Sciences, Arizona State University, Tempe, AZ, 85287, United States

ARTICLE INFO

Editor: DR J BADRO

Keywords:
Mars
Core formation
Dihedral angles
Majorite garnet
Ringwoodite
Highly siderophile elements (HSEs)

ABSTRACT

Geochemical constraints imply that a solid silicate layer existed between the base of the Martian magma ocean (~14 GPa) and the core-mantle boundary (~18–20 GPa) during early differentiation. Both S-poor metallic melts segregated during core formation and S-rich sulfide melts exsolved upon subsequent magma ocean cooling must have percolated through this layer to the core, but the efficiency of this process is poorly constrained. At ~18 GPa, this layer comprises roughly equal proportions of ringwoodite and majorite garnet, yet no dihedral angles in majorite garnet have been reported. We conducted experiments at 18 GPa and 1723–2200 K to determine dihedral angles between Fe(-Ni)-S-O alloy melts (25–46 mol% S+O) and both ringwoodite and majorite garnet. Dihedral angles decrease with increasing temperature, S+O content, and oxygen fugacity, while Ni has no effect. Dihedral angles in majorite garnet are systematically ~10° lower than in ringwoodite under comparable conditions. Despite this, all dihedral angles (89°-126°) remain above the 60° threshold for melt interconnection, so the entire mineral assemblage acts as a percolation barrier. Because our experimental S+O contents exceed those of the S-poor core-forming alloy (~15 mol% S), the measured angles represent a lower bound; the barrier for core-forming metal was even more severe. Theoretical models predict that for such angles, a few (> ~1–2) vol.% of melt remains trapped as isolated pockets upon network disconnection. Such melts constitute a hidden deep mantle reservoir of highly siderophile elements (HSEs) and siderophile volatiles (C, N), explaining their abundances in bulk silicate Mars without requiring a late veneer.

1. Introduction

In recent years, our understanding of the internal structure of Mars has advanced significantly owing to seismic observations from the InSight mission (Huang et al., 2022; Irving et al., 2023; Stähler et al., 2021). However, the present-day interior structure of Mars does not simply reflect its current state; rather, it is largely controlled by early differentiation processes such as core-mantle segregation and the crystallization of a magma ocean that occurred following planetary accretion (Bouvier et al., 2018; Kruijer et al., 2017). For terrestrial planets such as Earth and Mars, large-scale magma oceans are thought to have formed during planetary accretion, likely by energetic processes such as giant impacts (Tonks and Melosh, 1993). As these magma oceans cooled and crystallized, metallic and sulfide melts segregated gravitationally from the silicate melts to form the metallic core. While it is well established that the Martian core formed rapidly within the first few million years of Solar System history (Kruijer et al., 2017; Tang and Dauphas, 2014), it remains unclear if metal-silicate separation was complete or whether a fraction of the metallic melt was trapped within the silicate mantle. This question has direct implications for the residual budget of siderophile and chalcophile elements in the Martian mantle and, by extension, for the geochemical evolution recorded in Martian meteorites.

Geochemical constraints from metal-silicate partitioning

* Corresponding authors.
E-mail addresses: kyusei.tsuno@yale.edu (K. Tsuno), damanveer.grewal@yale.edu (D.S. Grewal).

https://doi.org/10.1016/j.epsl.2026.120246
Received 21 April 2026; Received in revised form 6 July 2026; Accepted 20 July 2026
Available online 25 July 2026

experiments suggest that core-mantle differentiation on Mars occurred at 14 ± 3 GPa, 2100 ± 200 K, and ΔIW (oxygen fugacity (fO_2) relative to the iron-wüstite buffer) = −1.5 to −0.5 (Rai and Van Westrenen, 2013; Righter and Chabot, 2011). These conditions are interpreted as the effective pressure-temperature of metal-silicate equilibration, which approximates the average depth of the Martian magma ocean. By contrast, seismic analyses from the InSight mission constrain the core-mantle boundary (CMB) to lie at pressures of 18–20 GPa (Huang et al., 2022; Khan et al., 2022; Stähler et al., 2021). The difference between these two pressure estimates implies that a solid layer, several hundred kilometers thick, existed between the base of the magma ocean and the CMB during early differentiation. Metallic melts that segregated from silicate melt within the magma ocean must therefore have subsequently migrated through the solid silicate mantle to reach the core.

A plausible mechanism for such migration is percolation, in which melt forms an interconnected network along grain boundaries and migrates through porous flow under gravity (Stevenson, 1990). The connectivity of these melt networks is governed by the solid-solid and solid-melt interfacial energies, whose ratio is expressed through the dihedral angle (θ):

$$2\cos\left(\frac{\theta}{2}\right) = \frac{\gamma_{ss}}{\gamma_{sm}} \quad (1)$$

where γ_{ss} and γ_{sm} are the solid-solid interfacial energy and solid-melt interfacial energy, respectively. When $\theta < 60^\circ$, an energetically stable, interconnected melt network forms even at very low melt fractions (Ghanbarzadeh et al., 2017; von Bargen and Waff, 1986). When $\theta > 60^\circ$, melts occur as isolated droplets at low melt fractions and require progressively higher melt fractions to achieve connectivity. Even where a network is temporarily established, pore-scale simulations show that melt connectivity is hysteretic: an interconnected network can drain down to a melt fraction of only ~1–2 vol.% before it disconnects, leaving at least this fraction stranded as isolated pockets (Ghanbarzadeh et al., 2017). The efficiency of percolative metal segregation through the solid Martian mantle therefore depends critically on the dihedral angle between the metallic melt and the surrounding silicate minerals.

The dihedral angles between metallic melts and silicate minerals are strongly controlled by the composition of the metallic melts, particularly the concentrations of surface-active non-metal elements such as S and O (Manilal et al., 2026; Terasaki et al., 2009). Higher S and O contents reduce the solid-melt interfacial energy (γ_{sm}), thereby lowering the dihedral angle and promoting wetting of grain boundaries. To predict the percolation behavior of metallic melts in the Martian mantle, it is therefore necessary to consider the S content of the Martian core. Early seismic analyses from the InSight mission suggested that 20–27 wt.% sulfur would be required to explain the low density of the Martian core (Huang et al., 2022; Irving et al., 2023; Stähler et al., 2021). However, the subsequent identification of a silicate melt layer directly above the CMB leads to a higher inferred core density (Khan et al., 2023; Samuel et al., 2023), and the estimated sulfur content of the Martian core has been revised down to 9–10 wt.% (Khan et al., 2023, 2022; Samuel et al., 2023). Even at this revised estimate, sulfur remains a major component of the Martian core, in stark contrast to Earth's core, where sulfur is a minor component (~2 wt.%; e.g., Dreibus and Palme, 1996). This high S content means that metallic melts percolating through the solid Martian mantle would have been S-rich, with direct consequences for their interfacial properties and wetting behavior.

Given that sulfur strongly controls the dihedral angle of metallic melts, and that the Martian core is relatively S-rich, understanding the percolation behavior of S-bearing metallic melts through the FeO-rich Martian mantle (14–18 wt.% FeO; Dreibus and Wänke, 1985; Taylor, 2013; Yoshizaki and McDonough, 2020) is essential for constraining the completeness of metal-silicate separation on Mars. Numerous studies have investigated the wetting behavior of S-rich metallic melts in silicate systems (Ballhaus and Ellis, 1996; Gaetani and Grove, 1999; Holzheid et al., 2000; Manilal et al., 2026; Miura et al., 2025; Rose and Brenan, 2001; Shannon and Agee, 1996, 1998; Terasaki et al., 2007, 2008; Wang and Fei, 2023). However, most were conducted either at relatively low pressures (<5 GPa) or at pressures exceeding 20 GPa, rather than at the intermediate pressures relevant to the Martian mantle. Terasaki et al. (2005) performed experiments under conditions relevant to the deep Martian mantle and reported dihedral angles of 79–102° for Fe-S alloy melts in ringwoodite at 20 GPa and 2200 K, suggesting incomplete melt extraction and possible melt trapping within the silicate matrix.

Critically, however, high-pressure phase equilibrium experiments on Martian mantle compositions show that ringwoodite and majorite garnet coexist in nearly equal proportions at pressures of ~18 GPa (Bertka and Fei, 1997; Duncan et al., 2018). Despite constituting approximately half of the mineral assemblage at the Martian CMB, the dihedral angle between metallic melts and majorite garnet has never been experimentally determined. This represents a fundamental gap in our understanding of melt percolation in the deep Martian mantle.

In this study, we conducted high-pressure experiments at 18 GPa to determine the dihedral angles of S-bearing Fe(-Ni) metallic melts in both ringwoodite and majorite garnet under conditions relevant to the deep Martian mantle. Using starting materials with compositions along the Fe-FeS join, we systematically examined the effects of sulfur content, temperature (1723–2200 K), fO_2 (controlled via the FeO content of the silicate), and Ni on the dihedral angle. We further evaluate the potential for trapped metallic and sulfide melts to serve as a hidden reservoir of highly siderophile elements (HSEs) and siderophile volatiles (C, N) in the deep Martian mantle and show that this mechanism can account for the Bulk Silicate Mars (BSM) HSE abundances that cannot be explained by equilibrium partitioning alone.

2. Experimental procedures

2.1. Starting materials

Starting materials consisted of mixtures of metallic and silicate components prepared from reagent-grade oxides, carbonates, and metal powders (see **Supplementary Information)**. Target bulk compositions are listed in Table 1. Metallic starting compositions were designed to contain 10 wt.% and 20 wt.% S, with Ni added where appropriate to evaluate the effects of metal composition on dihedral angle. Silicate starting compositions were chosen to reproduce ringwoodite- and majorite-bearing assemblages relevant to the deep Martian mantle, following the high-pressure phase equilibrium experiments of Bertka and Fei (1997). Metallic and silicate components were mixed to yield a metallic melt fraction of 2 vol.%, comparable to or lower than the critical melt fraction required for melt connectivity when dihedral angles exceed 60° (von Bargen and Waff, 1986).

2.2. High-pressure experiments

Experiments were conducted at 18 GPa and temperatures of 1723, 1873, and 2200 K using a Kawai-type multi-anvil apparatus at the Geodynamics Research Center (GRC), Ehime University and at the Facility for Open Research in a Compressed Environment (FORCE), Arizona State University (ASU). These pressure and temperature conditions were selected to reproduce the conditions in the solid silicate layer between the base of the Martian magma ocean and the CMB, based on: (i) the inferred CMB depth from InSight seismology (Huang et al., 2022; Irving et al., 2023; Khan et al., 2023; Samuel et al., 2023; Stähler et al., 2021), (ii) experimental constraints on the Martian mantle solidus (Duncan et al., 2018), and (iii) the *P-T* conditions of metal-silicate equilibration in the magma ocean inferred from metal-silicate melt partitioning of moderately siderophile elements (Rai and Van Westrenen, 2013; Righter and Chabot, 2011). The lowest temperature (1723 K) lies well below the estimated Martian mantle solidus at 18 GPa,

Table 1
Experimental conditions and phase assemblages.

Run No.[a]	T (K)	Duration (h)	Capsule	Alloy[b]	Silicate[c]	Oxygen fugacity			Dihedral angle			
						ΔIW[d]	+Error	-Error	Counts	median	Upper CI[e]	Lower CI[e]
(Starting mix: alloy plus ringwoodite composition)												
OT3114–1	1723	12	MgO	Fe-20S	Rw	−0.82	0.09	0.1	167	125.9	128.2	122.9
OT3114–2	1723	12	MgO	Fe-10Ni-20S	Rw	−0.7	0.07	0.08	203	123.1	124.6	119.6
OT3109–1	1873	12	MgO	Fe-10S	Rw	−0.88	0.06	0.06	247	120.5	123.0	116.9
OS4001–1	1873	12	MgO	Fe-20S	Rw	−1.14	0.05	0.06	266	113.2	114.5	110.2
OS4001–2	1873	12	MgO	Fe-20S	Rw (low FeO)	−1.26	0.06	0.06	316	112.9	115.1	110.3
OT3175	1873	12	Graphite	Fe-20S	Rw	−0.8	0.05	0.06	149	104.0	107.7	99.8
J11	2200	3	Graphite	Fe-20S	Rw	−0.69	0.06	0.06	182	94.0	96.0	90.5
(Starting mix: alloy + majorite garnet composition)												
OT3114–3[f]	1723	12	MgO	Fe-20S	Grt	−1.34	0.07	0.08	283	117.2	119.7	112.7
OT3109–2[f]	1873	12	MgO	Fe-10S	Grt	−0.95	0.06	0.07	155	115.5	117.7	112.9
OS4001–3[f]	1873	12	MgO	Fe-20S	Grt	−1.47	0.12	0.15	249	107.4	109.5	104.2
OS4002–3[f]	1873	12	MgO	Fe-10Ni-20S	Grt	−1.32	0.05	0.06	166	105.1	107.4	101.4
OT3178	1873	12	Graphite	Fe-20S	Grt	−0.82	0.09	0.11	235	98.2	100.4	94.4
J8	1873	3	Graphite	Fe-20S	Grt	−0.72	0.1	0.12	220	88.6	90.0	84.9

[a] Experiments with run numbers OT and OS were conducted using ORANGE-2000 or -3000 at GRC, Ehime University, whereas those with run numbers starting with J were performed using the Jasmine at FORCE, Arizona State University.
[b] Alloy starting composition (wt.%). For example, Fe-10Ni-20S contains 10 wt.% Ni and 20 wt.% S, with the remainder Fe.
[c] Silicate starting compositions (wt.%): 25.4 FeO (Rw: ringwoodite), 14.4 FeO (low FeO Rw), and 51.4 SiO_2, 7.38 Al_2O_3, 9.85 FeO, 5.68 CaO, 24.5 MgO, and 0.83 Na_2O (Grt: majorite garnet).
[d] Oxygen fugacity relative to iron-wüstite buffer.
[e] 95% confidence interval.
[f] Rw is present at the capsule margin.

whereas 2200 K approaches it from above, so that experiments span the plausible thermal range of the solid silicate layer during early differentiation. Run durations were 12 h at 1723–1873 K and 3 h at 2200 K (Table 1), based on previous studies demonstrating that textural equilibrium is achieved under comparable conditions (Shannon and Agee, 1996; Terasaki et al., 2005). Details of the cell assemblies, experimental setup, and pressure calibration procedures are provided in the **Supplementary Information** and **Supplementary Fig. 1**.

2.3. Analysis of recovered samples

Textural observations were conducted using a field-emission scanning electron microscope (FE-SEM; JEOL JSM-IT500HR) and a field-emission electron probe microanalyzer (FE-EPMA; JEOL JXA-iHP200F) at GRC, as well as a JEOL JXA-8530F FE-EPMA at ASU. Dihedral angles were measured from backscattered electron (BSE) images using ImageJ. Median values were used to represent each sample, with uncertainties reported as 95% confidence intervals. The use of the median follows the standard approach of Jurewicz and Jurewicz (1986) and is consistent with previous studies (Gaetani and Grove, 1999; Manilal et al., 2026; Miura et al., 2025; Rose and Brenan, 2001; Shannon and Agee, 1996; Terasaki et al., 2005, 2008). A total of 149–316 measurements were obtained for each sample (Table 1). Major element compositions were determined by wavelength-dispersive spectroscopy (WDS) using the ASU JEOL JXA-8530F at a 15 kV accelerating voltage and a 15 nA beam current. Beam diameters were 1 μm for silicate phases and 1–5 μm for metallic phases to account for compositional heterogeneity. Analytical procedures, standards, and correction methods are described in the **Supplementary Information**.

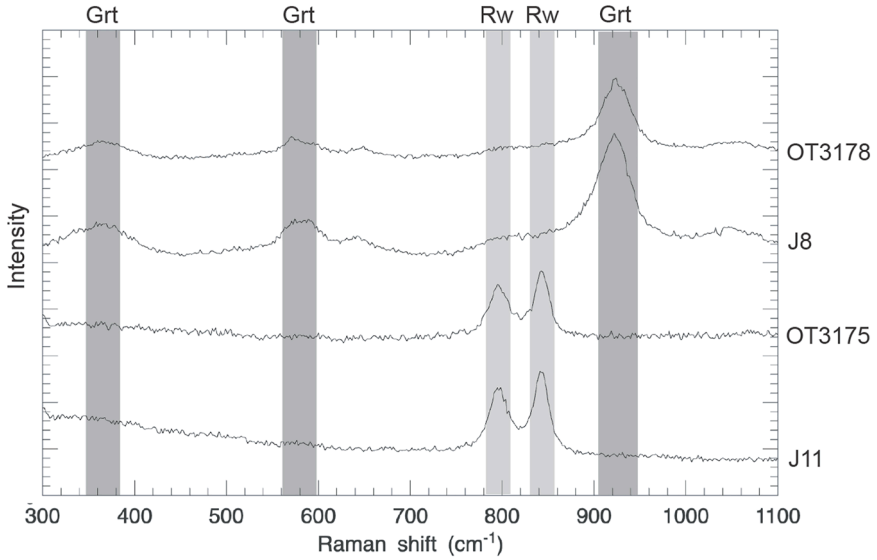

Fig. 1. Raman spectra of representative experimental samples. The gray shaded bands indicate the positions of characteristic vibrational modes of majorite garnet (Grt) and ringwoodite (Rw). The spectra are vertically offset for clarity.

3. Experimental results

3.1. Textural observation and phase identification

Raman spectroscopic analyses show that in experiments conducted using MgO capsules, the ringwoodite starting composition yielded single-phase ringwoodite (Fig. 1), whereas the majorite-garnet starting composition produced majorite, with ringwoodite forming along the inner capsule walls (**Supplementary Fig. 2**). The reaction rim is interpreted to have formed via the reaction: MgO (capsule) + $MgSiO_3$ (majorite) = Mg_2SiO_4 (ringwoodite). This reaction is restricted to the capsule interface and does not significantly influence melt distribution within the sample interior. Dihedral angles were measured only in the interior region, away from the capsule wall, to avoid any potential boundary effects. By contrast, experiments performed using graphite (diamond) capsules yielded ringwoodite from the ringwoodite starting composition and single-phase majorite garnet from the majorite-garnet starting composition (Fig. 1).

Back-scattered electron (BSE) imaging of the recovered samples shows that, in both MgO and graphite (diamond) capsule experiments, metallic melt is distributed along grain boundaries and triple junctions of ringwoodite or majorite garnet (Fig. 2). The metallic melt predominantly occurs as isolated pockets localized at grain-boundary triple junctions, consistent with textural equilibrium. No elongated or interconnected melt networks were observed in any of the experiments. Representative microstructures of experiments conducted at 1723 K and 1873 K are shown in Figs. 2a and 2b. In ringwoodite-bearing samples, metallic melt forms isolated pockets with clearly obtuse internal angles (Fig. 2a). In garnet-bearing samples, although some melt pockets exhibit obtuse angles, acute angles are more frequent (Fig. 2b), consistent with the systematically lower dihedral angle distributions in the garnet system (Section 3.4). In graphite capsule experiments, where a larger amount of FeO was retained in the sample (see Section 3.2.2 for further discussion of capsule effects on FeO content of the silicate minerals), more acute dihedral angles are observed in both ringwoodite and garnet samples (Figs. 2c and 2d). A small amount of ferropericlase was also observed in the ringwoodite samples under these conditions (Fig. 2c).

Grain sizes of ringwoodite at 1723–1873 K in MgO capsule experiments (~12–16 wt.% FeO) are ~5–15 μm (Fig. 2a), whereas in graphite capsule experiments at 1873–2073 K (~27 wt.% FeO), they increase to ~20–50 μm (Fig. 2c), with maxima up to ~80 μm. FeO-rich ringwoodite exhibits markedly larger grain sizes, likely owing to the effect of FeO content on grain-growth kinetics controlled by atomic diffusion in silicate minerals (Chakraborty, 2010). Grain sizes of garnet at 1723 K and 1873 K using MgO capsules are comparable to those of ringwoodite (Fig. 2b), but remain smaller (~5–25 μm) at higher temperatures in graphite capsule experiments (Fig. 2d) than those of ringwoodite, possibly owing to slower diffusion-controlled grain growth in majorite garnet (van Mierlo et al., 2013). These differences do not affect the measured dihedral angles, which are governed by interfacial energies (Eq. (1)) and are independent of grain size under textural equilibrium conditions (von Bargen and Waff, 1986).

3.2. Phase composition

The chemical compositions of the metallic melts and silicate minerals are listed in **Supplementary Tables 1 and 2**, respectively. Compositions are reported in wt.% in this section and converted to mol% for subsequent thermodynamic calculations.

3.2.1. Metallic melt composition

MgO capsule experiments at 1723 K with the 20 wt.% S starting material produced metallic melts containing 19.2–24.0 wt.% S and 0.32–0.53 wt.% O. At 1873 K, metallic melts contain 15.8–19.8 wt.% S and 0.21–0.32 wt.% O for the 10 wt.% S starting compositions, and 24.7–30.3 wt.% S and 0.56–0.63 wt.% O for the 20 wt.% S starting

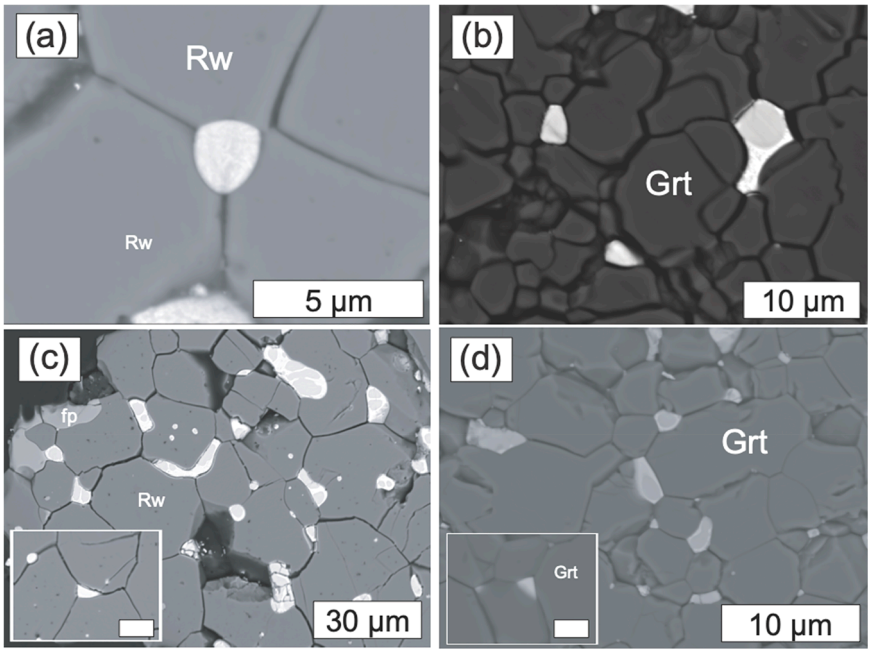

Fig. 2. Backscattered electron (BSE) images of representative samples recovered from high-pressure and high-temperature experiments. The bright phase corresponds to Fe(-Ni)-S alloy melt, whereas the dark gray phases represent coexisting silicate minerals (Rw: ringwoodite; Grt: garnet; Fp: ferropericlase). The melt is mainly distributed along grain boundaries and triple junctions. **(a, b)** Samples synthesized in MgO capsules at 1723–1873 K, in which the FeO content of the silicate phase is low: **(a)** OT3114–1 (1723 K; ringwoodite system) and **(b)** OS4001–3 (1873 K; garnet system). In the ringwoodite system, the alloy melt exhibits relatively rounded morphologies, whereas in the garnet system, more acute dihedral angles are observed. **(c, d)** Samples recovered from experiments conducted in graphite capsules, characterized by higher FeO contents in the silicate phase: **(c)** J11 (2200 K; ringwoodite system), inset: texture showing relatively small dihedral angles (scale bar: 2 μm); **(d)** J08 (2200 K; garnet system), inset: similar textures with small dihedral angles (scale bar: 2 μm). The grain size in the ringwoodite system is generally larger than that in the garnet system, and the alloy melt pockets tend to be larger. Scale bars are shown in each panel.

compositions. In all cases, sulfur contents are higher than those of the starting compositions, likely because of Fe loss to the MgO capsule, which enriches the residual melt in S. Oxygen content increases with sulfur content, consistent with the thermodynamic coupling between S and O solubility in Fe-alloy melts at high pressure (see Section 4.1). In graphite (diamond) capsule experiments, the 20 wt.% S starting compositions yielded metallic melts containing 30.3–30.6 wt.% S and 0.68–0.81 wt.% O at 1873 K, and 27.9–29.8 wt.% S and ~1.1 wt.% O at 2200 K. Sulfur contents are consistently higher than those of the starting compositions, likely reflecting Fe loss to coexisting silicates. Oxygen content increases with temperature. No systematic difference in oxygen solubility was observed between ringwoodite- and garnet-bearing systems (see Section 4.1); thus, all data, including Ni-free and Ni-bearing experiments, are treated together. In all experiments, the Si content of the metallic melt ranged from 0.04 to 0.20 wt.%, and the Mg content ranged from 0.04 to 0.18 wt.%. These low values confirm that the measured metallic melt compositions are not significantly affected by analytical overlap with adjacent silicate grains.

3.2.2. Silicate composition

For the ringwoodite system, experiments in MgO capsules at 1723–1873 K produced ringwoodite containing 12.0 wt.% FeO from starting compositions with 14.4 wt.% FeO, and 14.2–16.0 wt.% FeO from starting compositions with 25.6 wt.% FeO. For the majorite garnet system, experiments in MgO capsules yielded garnet with markedly higher Al_2O_3 contents (~13.3–15.6 wt.%) and lower FeO (~3.4–4.1 wt.%) than the starting materials. This enrichment in Al_2O_3 reflects coexistence with ringwoodite formed by reaction with the MgO capsule, which preferentially extracts MgO and SiO_2 from the garnet and shifts the residual garnet composition toward higher Al_2O_3. In both systems, silicate FeO contents are generally lower than those in the starting materials, owing to FeO diffusion into the capsule walls.

By contrast, silicate compositions in graphite (diamond) capsule experiments are largely consistent with the starting materials. Ringwoodite contains ~27 wt.% FeO, and garnet compositions are also similar to the starting materials because graphite (diamond) is chemically inert with respect to silicate minerals. The preservation of higher FeO contents in the graphite capsule experiments imposes a substantially higher fO_2 than in the MgO capsule experiments (Section 3.3). This contrast provides the compositional leverage to evaluate whether fO_2, and the associated silicate FeO content, significantly influences the dihedral angles.

3.3. Oxygen fugacity between alloy melt and coexisting minerals

fO_2 was calculated relative to the iron-wüstite buffer (ΔIW) from the compositions of the Fe(-Ni)-S melt and coexisting ferropericlase (See **Supplementary Information**), following the method of Mann et al. (2009). Because ferropericlase was not present in most run charges, its FeO content was estimated from silicate compositions. For ringwoodite-bearing experiments, this was derived from ringwoodite compositions using an empirical relation (Tsuno et al., 2024). For garnet-bearing experiments, ringwoodite compositions were estimated from garnet composition using an Fe-Mg exchange coefficient (Bertka and Fei, 1997; Duncan et al., 2018; Frost, 2003; Nishihara and Takahashi, 2001) (**Supplementary Fig. 3**) and subsequently converted to ferropericlase compositions (see **Supplementary Information**).

For ringwoodite starting compositions, ΔIW values range from −1.26 to −0.70 in MgO capsule experiments and from −0.80 to −0.69 in graphite capsule experiments; for garnet starting compositions, they range from −1.47 to −0.95 and from −0.80 to −0.72, respectively. Overall, the experiments span ΔIW = −1.5 to −0.7, encompassing the range estimated for Martian core-mantle differentiation (ΔIW = −1.5 to −0.5; Rai and Van Westrenen, 2013; Righter and Chabot, 2011). This range is also broadly consistent with fO_2 estimates from Martian meteorites, which record values just below the IW buffer (e.g., Yamato 980459, QUE 94201, and ALH 84001; Karner et al., 2007; Righter, 2025), although these reflect younger igneous processes and may not directly represent conditions during core formation.

3.4. Dihedral angles between Fe(-Ni)-S melt and coexisting silicate minerals

The distributions and median values of dihedral angles are presented in Table 1 and Fig. 3. The relationships between dihedral angle, ΔIW, and S + O (mol%) are shown in Fig. 4. Before describing the systematics, we note that when the total S + O content is 25–32 mol%, dissolved oxygen contents are low (~1 mol%), whereas even at higher S + O contents (≥37 mol%), oxygen contents remain limited to ~1.6–3.1 mol % (Fig. 4a). These values indicate that the oxygen content is much smaller than the sulfur content and is also markedly lower than oxygen solubilities reported in previous low-pressure studies (Manilal et al., 2026; Minarik et al., 1996; Miura et al., 2025; Terasaki et al., 2008). Therefore, the effect of oxygen on the dihedral angle cannot be clearly distinguished from that of sulfur, and the total S + O content is used as the compositional parameter hereafter when evaluating the effect of anions on dihedral angle.

For the ringwoodite system (Fig. 4b), the addition of 11.2 mol% Ni at 1723 K has no measurable effect on the dihedral angle. At low S + O contents (30–32 mol%), dihedral angles show little variation (~120–126°) at 1723 K and 1873 K, but decrease markedly to ~104–113° at higher S + O contents (43–46 mol%) at 1873 K, with values decreasing with increasing fO_2. At 2200 K, the dihedral angle decreases further to ~95°, indicating a systematic decrease with increasing temperature. This value is consistent with the trend reported by Terasaki et al. (2005) at 20 GPa.

For the majorite garnet system (Fig. 4c a Ni-bearing metallic melt (38.1 ± 6.6 mol% S + O) at 1873 K exhibits dihedral angles (~105–107°) comparable to those of Ni-free melts (44.2 ± 7.3 mol% S + O) at similar fO_2 conditions. Dihedral angles show systematic dependencies on temperature and fO_2: at 37–38 mol% S + O, the dihedral angle at 1723 K (~117°) is higher than that at 1873 K (~105°), indicating an increase with decreasing temperature. At 1873 K and 43–46 mol% S + O, dihedral angles decrease from ~117° to ~98° with increasing fO_2, consistent with the effect observed in the ringwoodite system. At 2200 K, dihedral angles further decrease to ~89° at comparable S + O contents, consistent with a decrease with increasing temperature.

Across all conditions investigated (25–32 mol% S + O and 43–46 mol % S + O at 1873 K, and 43–46 mol% S + O at 2200 K), the dihedral angles of Fe(-Ni)-O-S melt in majorite garnet are systematically lower than those in ringwoodite, by up to ~10°, under comparable conditions (Fig. 4a). This offset represents the first experimental demonstration that the host mineral phase itself exerts a measurable control on the wetting behavior of S-rich metallic melts at deep Martian mantle conditions. Unlike Shannon and Agee (1998), who measured dihedral angles in a bridgmanite-dominated assemblage in which majorite garnet occurred only as a minor accessory phase, our study compares ringwoodite and majorite garnet directly, each as the major mineral phase. Despite the lower dihedral angles in garnet, all measured values remain well above the 60° threshold for interconnected melt networks at low melt fractions, indicating that neither ringwoodite nor majorite garnet permits efficient percolation of S-rich metallic melts under the conditions of this study.

4. Discussion

4.1. Oxygen solubility in Fe(-Ni)-S alloy melt coexisting with silicate minerals

The oxygen content of the alloy melt is important for two reasons.

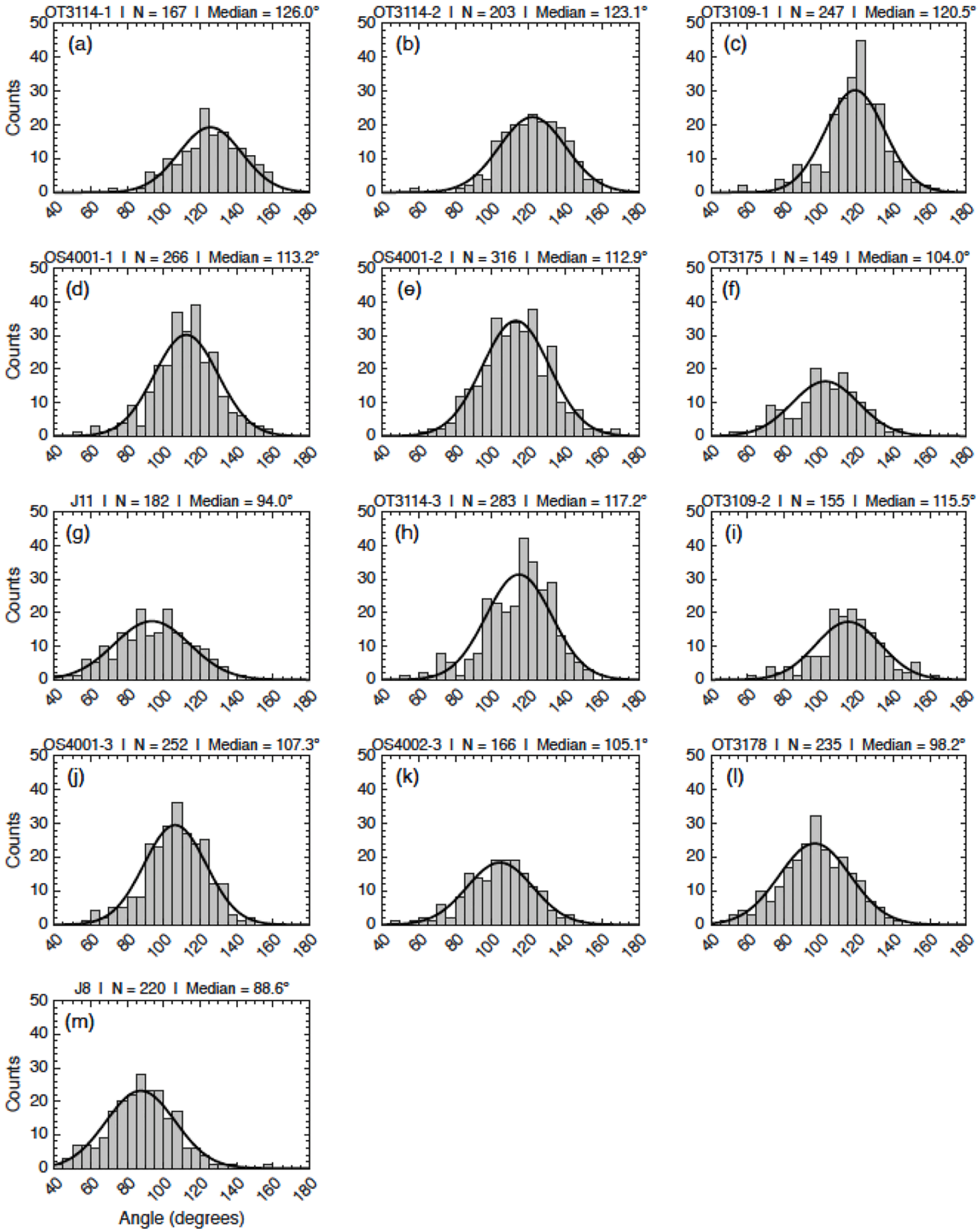

Fig. 3. Frequency distributions of measured dihedral angles for individual experimental samples. Histograms show the number of measurements as a function of dihedral angle, and solid curves represent Gaussian fits to the data. The total number of measurements (N) and the median value for each sample are indicated in each panel. The median is used as the representative dihedral angle throughout this study because dihedral angle distributions are typically positively skewed, making the median more robust than the mean. Panels **(a–g)** show dihedral angle distributions of alloy melts in ringwoodite, whereas panels **(h–m)** show those in garnet.

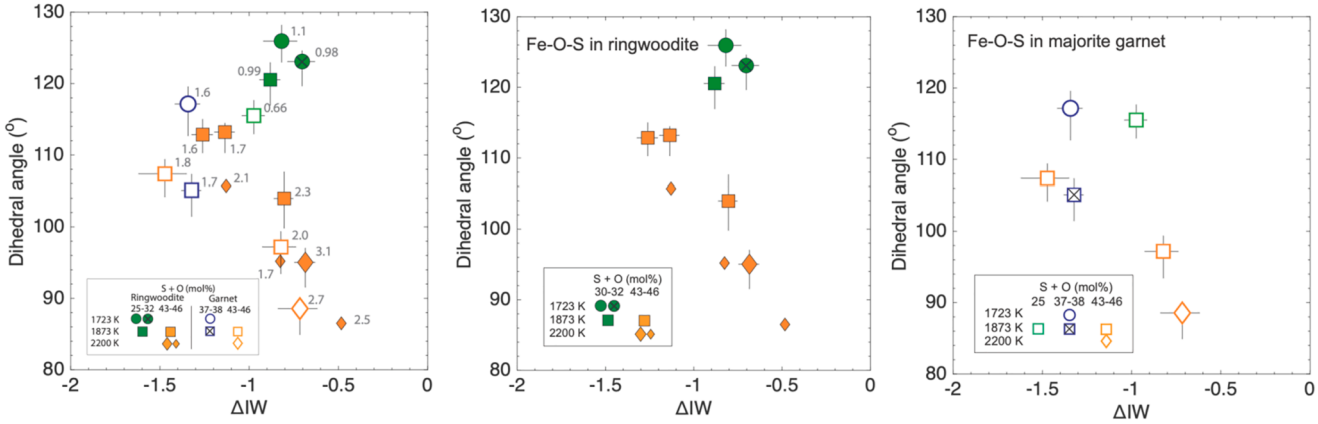

Fig. 4. Dihedral angles of Fe(-Ni)-S melt plotted against ΔIW for (**a**) all data, (**b**) the ringwoodite system, and (**c**) the majorite garnet system. Solid symbols represent measurements in ringwoodite, open symbols represent those in garnet. Circles, squares, and diamonds correspond to experiments conducted at 1723 K, 1873 K, and 2200 K, respectively. Data are color-coded according to the total S + O content (mol%) of the alloy melt: 25–32 mol% (green), 37–38 mol% (blue), and 43–46 mol% (orange). Symbols marked with an "X" indicate Ni-bearing alloys. Error bars represent 95% confidence intervals on the median. In panel (**a**), numbers next to symbols indicate the dissolved oxygen content (mol%) in the alloy melt, showing that O remains a minor component relative to S across the full experimental range. Dihedral angles in majorite garnet (open symbols) are systematically ~10° lower than in ringwoodite (solid symbols) at comparable ΔIW and S + O conditions. All measured values remain above 60°.

First, oxygen, like sulfur, is a surface-active element in metallic melts, and its presence contributes to lowering the solid-melt interfacial energy and hence the dihedral angle (Manilal et al., 2026; Terasaki et al., 2005). Second, the oxygen content is thermodynamically coupled to the sulfur content and to fO_2, such that characterizing this coupling is necessary to correctly attribute the observed dihedral angle variations to their underlying compositional and thermodynamic controls. The oxygen solubility data obtained in this study are summarized in Fig. 5. Within the investigated conditions, Ni has no measurable effect on oxygen solubility in S-bearing metallic melts. For example, oxygen solubility is ~1 mol % in the ringwoodite system (~30 mol% S, ΔIW ~ −0.9 to −0.7) and ~1.6–1.7 mol% in the garnet system (~37 mol% S, ΔIW ~ −1.3), with no systematic difference between Ni-free and Ni-bearing experiments.

No systematic difference is also observed between ringwoodite- and garnet-bearing systems. For example, for metallic melts containing ~41–43 mol% S at ΔIW ~ −1.2, oxygen solubility is ~1.6–1.7 mol% in both assemblages. Similarly, for metallic melts containing ~43–44 mol % S, oxygen solubility is ~2.0–2.3 mol% at ΔIW ~ −0.8, whereas for melts containing ~39–41 mol% S at ΔIW ~ −0.7, it is ~2.7–3.1 mol%, with comparable values obtained in both mineral assemblages. This similarity indicates that oxygen partitioning is primarily controlled by the thermodynamic properties of the Fe-S metallic melt and the imposed fO_2, and that the influence of the coexisting silicate mineralogy is minor, likely because FeO activities in ringwoodite and majorite garnet are broadly comparable under the conditions of this study.

Based on these observations, oxygen solubility (X_O: mole fraction) was parameterized as a function of temperature (T), oxygen fugacity (ΔIW), and sulfur content (X_S: mole fraction), by combining data from both systems. The resulting empirical relationship is:

$$ln(X_O) = -0.235(\pm 0.670) - 3400(\pm 1492)/T + 0.186(\pm 0.197) \times \Delta IW + 1.93(\pm 0.31) \times ln(X_S) \quad (R^2 = 0.903) \quad (2)$$

Eq. (2) shows that, within the experimental range of this study, X_O

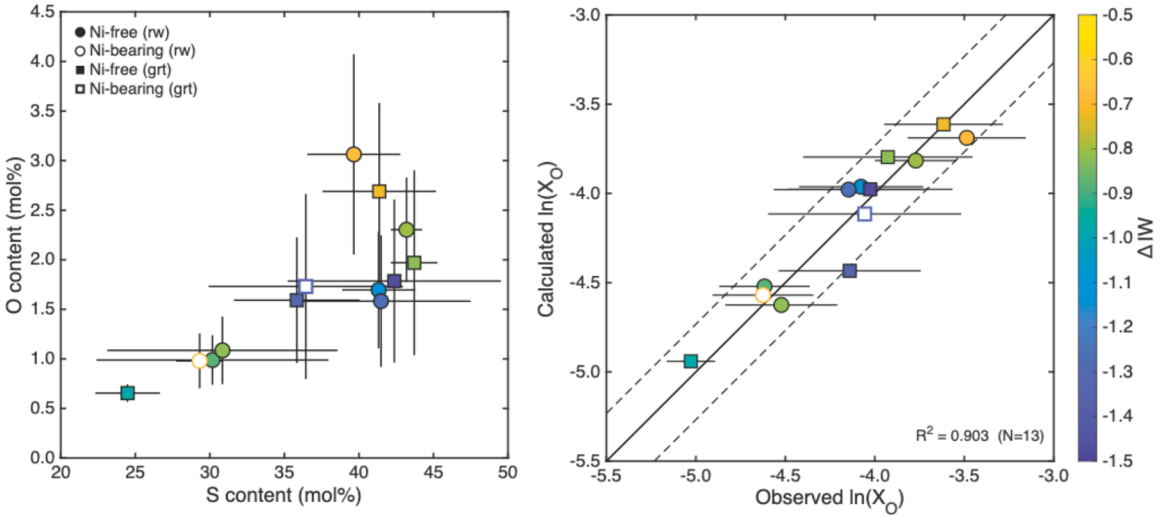

Fig. 5. **(a)** Oxygen content in Fe–S melts expressed in mol% as a function of sulfur content (mol%) for experiments in both the ringwoodite (rw) and garnet (grt) systems. Filled and open symbols denote Ni-free and Ni-bearing alloys, respectively. Error bars represent analytical uncertainties. **(b)** Comparison between observed and calculated values of $\ln(X_O)$, where X_O is the oxygen solubility expressed as a mole fraction, based on the empirical regression given in Eq. (2). The solid line represents the 1:1 relationship, and the dashed lines indicate the 95% confidence interval. Colors correspond to ΔIW values, as shown by the color scale. The coefficient of determination is $R^2 = 0.903$ (N = 13).

increases with increasing T and X_S, whereas the effect of fO_2 is comparatively minor. The high goodness of fit ($R^2 = 0.903$) indicates that the present dataset is internally consistent and that the dominant thermodynamic controls are well constrained under the investigated conditions. The strong positive dependence of X_O on X_S (coefficient = 1.93 ± 0.31) implies that, under the high-pressure conditions of this study, oxygen and sulfur contents in the metallic melt are positively coupled. Because both elements are surface-active, their combined effect on the dihedral angle is captured by the total S + O content, as adopted in Section 3.4. The weak dependence on the ΔIW term indicates that fO_2 affects the dihedral angle primarily through its control on the FeO content of the coexisting silicate phase (which determines γ_{sm}), rather than through changes in the oxygen content of the metallic melt. To examine whether this relationship can be extended beyond the present experiments, we compiled previously published oxygen solubility and partitioning data obtained under comparable high-pressure conditions (**Supplementary Fig. 4**), and the details and comparison with this study are discussed in the **Supplementary Information**.

4.2. Controls on dihedral angle: effects of S + O, temperature, fO_2, and host silicate phase

The present results show that the dihedral angle of Fe(-Ni)-S melts is controlled by four variables: (1) the S + O content of the metallic melt, (2) fO_2, (3) temperature, and (4) the identity of the host silicate mineral. The dihedral angle systematically decreases with increasing S + O content, fO_2, and temperature. In addition, under comparable conditions, the majorite garnet system consistently yields lower dihedral angles (~10° lower) than the ringwoodite system. The first three dependencies are consistent with, and extend to higher pressures, the trends reported in previous experimental studies on Fe-S melts at lower pressures (Ballhaus and Ellis, 1996; Gaetani and Grove, 1999; Terasaki et al., 2005, 2008). The fourth is a new finding of this study. We discuss each of these controls and their physical origins below.

4.2.1. Effects of S + O content and temperature

Sulfur and oxygen are well-known surface-active elements in metallic melts, and experimental studies have shown that increasing their contents lowers the metal-silicate interfacial energy (γ_{sm}) (Manilal et al., 2026; Terasaki et al., 2009). This reduces γ_{sm} and, through Eq. (1), lowers the dihedral angle. In general, interfacial free energy decreases with increasing temperature, and the temperature dependence observed in this study is consistent with such thermodynamic behavior. The combined effect of S + O content and temperature is substantial. In the ringwoodite system, the dihedral angle decreases from ~126° at low S + O content and low temperature (32 mol% S + O, 1723 K) to ~94° at high S + O content and high temperature (46 mol% S + O, 2200 K), corresponding to a reduction of ~32°. Similarly, in the majorite garnet system, the dihedral angle decreases from ~117° at low S + O and low temperature (37 mol% S + O, 1723 K) to ~89° at high S + O and high temperature (46 mol% S + O, 2200 K), corresponding to a reduction of ~28°.

4.2.2. Effect of fO_2

An increase in the FeO content in the silicate phase, which is the primary compositional consequence of increasing fO_2 in these experiments, reduces the chemical contrast between the metallic melt and the surrounding silicate minerals. The higher Fe^{2+} concentration enhances chemical affinity across the interface, thereby lowering γ_{sm}. As shown in Section 4.1, the effect of fO_2 on the oxygen content of the alloy melt is comparatively minor, confirming that fO_2 influences the dihedral angle primarily through its control on the silicate side of the interface rather than through the metallic melt composition.

4.2.3. Effect of the host silicate mineral: majorite garnet versus ringwoodite

The systematic difference in dihedral angle between the ringwoodite and majorite garnet systems is unlikely to arise from differences in metallic melt composition, as comparisons were made under closely matched fO_2 and S + O contents in the metallic melt. Instead, this difference likely reflects variations in interfacial and/or grain-boundary energetics inherent to the mineral structure. Majorite garnet is a multi-component phase that accommodates a wide range of cation substitutions (Mg^{2+}, Fe^{2+}, Ca^{2+}, Na^{+}, Al^{3+}, Si^{4+}) across multiple crystallographic sites, including both the dodecahedral (X) and octahedral (Y) sites. This chemical and structural diversity may facilitate local structural relaxation and charge compensation at the solid-melt interface, potentially lowering γ_{sm}. In particular, the presence of Ca^{2+} and Na^{+} in the garnet structure may create a more heterogeneous surface charge distribution that promotes wetting by the metallic melt. As a result, the dihedral angle is expected to decrease (Eq. (1)). By contrast, ringwoodite, with its spinel-type structure, has more limited cation substitution mechanisms - essentially restricted to Fe^{2+}-Mg^{2+} exchange on a single octahedral site - and therefore likely exhibits less structural adaptability at the interface.

Because the dihedral angle depends not only on the solid-melt interfacial energy (γ_{sm}) but also on the grain-boundary energy (γ_{ss}) (Eq. (1)), the structural complexity of majorite garnet may also affect γ_{ss}, though the direction and magnitude of this effect remain uncertain. If the multi-component nature of garnet also raises γ_{ss} (i.e., garnet grain boundaries are relatively high-energy), then the observed dihedral angle reduction may underestimate the decrease in γ_{sm} alone. Future studies combining dihedral angle measurements with direct determinations of interfacial and grain-boundary energies (for instance, through contact-angle experiments or molecular dynamics simulations) would help disentangle these contributions.

We note that the majorite garnet compositions in the MgO capsule experiments are enriched in Al_2O_3 (~13–16 wt.%) relative to Martian mantle majorite estimates (~2–5 wt.% Al_2O_3; Bertka and Fei, 1997) owing to reaction with the capsule (Section 3.2.2). However, this compositional shift does not undermine the key finding. The ~10° dihedral angle reduction relative to ringwoodite is observed at matched fO_2 and S + O conditions in the alloy melt, meaning the comparison isolates the effect of the host mineral structure. Moreover, the graphite capsule experiments produced garnet compositions closer to the starting materials (**Supplementary Table 2**) and yield dihedral angles consistent with the same ~10° offset, confirming that the result is not an artifact of Al-enrichment. If anything, lower-Al Martian majorite, being closer in composition to pyroxene, might exhibit even lower dihedral angles, making our measurements conservative in this respect as well.

4.2.4. Extrapolation to Martian core-forming compositions

The metallic melt compositions investigated in this study (25–46 mol % S + O) span a range directly relevant to the S-rich sulfide melts (~50 mol% S) exsolved during magma ocean cooling, but greatly exceed the S content of the primary core-forming alloy (~15 mol% S, corresponding to ~9 wt.% S in the Martian core). Because increasing S + O content systematically lowers the dihedral angle (Section 3.4), the S-poor core-forming alloy would have had higher dihedral angles than those measured here. For instance, the highest dihedral angles observed here (~120–126° at 30–32 mol% S + O, 1723 K and 1873 K in ringwoodite) already substantially exceed 60°, and alloy melts with ~15 mol% S would be expected to have even larger dihedral angles. Our measured values therefore provide conservative lower bounds on the dihedral angles relevant to the primary stage of Martian core formation.

Conversely, for the S-rich sulfide melts exsolved after magma ocean cooling, the experimental trend (Fig. 4a) indicates that even at the highest S + O contents investigated (~46 mol%), dihedral angles remain ~89–94°, still well above 60°. Modest extrapolation to ~50 mol% S (pure FeS) suggests dihedral angles of ~80–90°, consistent with Terasaki et al. (2005) at 20 GPa. Thus, both the S-poor and S-rich

metallic melts relevant to Martian differentiation would have been impeded by the percolation barrier identified in this study.

4.3. Melt transport through the solid silicate mantle: percolation, diapirism, and deformation

Percolation and diapirism are complementary pathways that operate at different scales of metal accumulation (Rubie and Jacobson, 2016; Stevenson, 1990). Core-forming metal that accumulates as a sufficiently thick pond at the base of the magma ocean becomes gravitationally unstable and descends through the solid mantle as a coherent diapir (Fleck et al., 2018), the dominant and faster mechanism for transporting the bulk of the core-forming metal. Metal that remains dispersed at the grain scale, below this critical accumulation, is instead governed by percolation physics (Wang and Fei, 2023). Our model concerns the fate of this residual, grain-scale melt left behind after the bulk of the metal had already descended to the core, rather than the bulk transport itself.

The fraction of this residual melt that remains trapped depends on hysteresis in melt connectivity (Ghanbarzadeh et al., 2017). Connectivity is first established, as melt fraction increases, at a percolation threshold that is substantially higher than the fraction at which an already-connected network loses connectivity during drainage; the latter trapping threshold lies at only ~1–2 vol.% at $\theta = 90°$. If a residual metal pond's initial melt fraction exceeded the percolation threshold, an interconnected network formed and subsequently drained to the ~1–2 vol.% trapping threshold; if it did not, the melt never established connectivity and was retained in full as isolated pockets. Which case applies depends on how efficiently diapirs formed, which is presently difficult to constrain; we therefore treat the trapped fraction as bounded below by ~1–2 vol.% and adopt this as a conservative value in Section 4.4.

Our estimates derive from textural-equilibrium experiments under static conditions, whereas the mantle deforms as it convects. Experimental studies of deformation-assisted connectivity disagree on whether low strain rates suppress or promote interconnection, and their laboratory strain rates (~10^{-4} s^{-1}) exceed those of mantle convection (~10^{-14} s^{-1} on Earth) by many orders of magnitude (Groebner and Kohlstedt, 2006; Walte et al., 2011; Wang and Fei, 2023), with the Martian value poorly constrained. Notably, Wang and Fei (2023) find nearly identical dihedral angles under static (~77°) and deformed (~79°) conditions, implying that any deformation-induced interconnection reflects differential stress overcoming interfacial tension rather than a lower equilibrium angle. This bears directly on the longevity of the trapped reservoir: if deformation transiently reconnects the network, trapped pockets could slowly drain and the reservoir's lifetime would be reduced, whereas if it does not, the reservoir persists over geological timescales, as assumed in Section 4.4.

4.4. Implications for highly siderophile elements and volatile retention in the Martian mantle

As demonstrated in Section 4.2, the deep Martian mantle acted as a percolation barrier for both the primary core-forming alloy and the S-rich sulfide melts exsolved during planetary differentiation; notably, the barrier would have been even more severe for the S-poor primary core-forming alloy (Section 4.2.4).

When $\theta > 60°$, metallic melt can still percolate if the melt fraction is sufficiently high, but a significant fraction becomes trapped as isolated pockets once the melt network disconnects during drainage. The magnitude of this trapped fraction is debated. Theoretical models based on idealized regular grains predict trapping at melt fractions of ~5–6 vol.% for $\theta > 60°$ (von Bargen and Waff, 1986), and experimental estimates for upper mantle silicate matrices suggest stranded melt fractions of 6–10 vol.% at high dihedral angles (Shannon and Agee, 1996). However, pore-scale simulations on irregular, realistic grain geometries show that hysteresis in melt network topology allows connected pathways to persist during drainage down to melt fractions of only ~1–2 vol.% (Ghanbarzadeh et al., 2017). We adopt 2 vol.% as a conservative lower bound in the calculations below, noting that the true trapped fraction may be substantially higher.

To evaluate the geochemical consequences of melt trapping, we consider the HSE budget of the Martian mantle. Using the parameterizations of Laurenz et al. (2016) and bulk Martian HSE abundances from ordinary and enstatite chondrites (Horan et al., 2003), we evaluate the HSE remaining in the Martian mantle after two sequential stages of differentiation (Fig. 6):

Stage 1: Fe-S alloy segregation. At 16 GPa and 2100 K, metal-silicate partition coefficients for an Fe-9 wt.% S alloy are on the order of 10^4–10^6 for the HSE (Laurenz et al., 2016), stripping the magma ocean to HSE concentrations of ≤0.08 ng/g – already ~8–18 times below BSM values (Yoshizaki and McDonough, 2020). This stage also leaves ~1300 μg/g S in the magma ocean, far exceeding the BSM estimate of 360 ± 120 μg/g (Wang and Becker, 2017).

Stage 2: Sulfide melt segregation. The excess sulfur requires removal through sulfide melt segregation upon magma ocean cooling, analogous to the "Hadean matte" (O'Neill, 1991; Rubie et al., 2016). The ~1300 μg/g S remaining after Stage 1 exceeds the sulfur concentration at sulfide saturation (SCSS) at 16 GPa and 2100 K, estimated at ~430 μg/g (Blanchard et al., 2021; Steenstra et al., 2022; ZhangZhou et al., 2024), so the magma ocean is sulfide-saturated and sulfide segregation is required rather than assumed. Because this SCSS value is comparable to the BSM sulfur estimate (Wang and Becker, 2017), sulfide segregation would draw mantle S down to levels consistent with BSM. We note, however, that no experimental calibration directly covers the combination of high pressure and high-FeO silicate melt composition relevant to the Martian mantle, so the specific SCSS value adopted here (~430 μg/g) carries an uncertainty that cannot presently be quantified (see **Supplementary Information**).

This sulfide melt further scavenges HSE, with sulfide-silicate partition coefficients of 10^3–10^4 (Laurenz et al., 2016). After both stages, the predicted HSE concentrations in the magma ocean are depleted by factors of ~50 (Pd) to ~12,000 (Ir) relative to BSM.

Equilibrium partitioning alone therefore cannot account for the HSE budget of BSM, and an additional mechanism is required. Trapped metallic melt in the solid silicate mantle provides such a mechanism. Assuming a conservative 2 vol.% of Fe-S alloy melt (Fe-9 wt.% S) is trapped, the resulting bulk silicate layer would contain ~127 ng/g Ru, 123 ng/g Pd, 172 ng/g Pt, and 84 ng/g Ir – concentrations that exceed BSM values by factors of 200–4500. Sulfide melt trapped during Stage 2 would add an additional ~1 ng/g Pd, with negligible contributions of the other HSEs. Although individual HSE differ in their metal- and sulfide-silicate affinities and in the temperature sensitivity of their partitioning (Laurenz et al., 2016), as reflected in the element-specific depletion and excess factors above, the trapped-melt reservoir over-supplies every HSE by at least ~200 × relative to BSM, so the mechanism is robust to element-to-element differences in the degree to which equilibrium was attained. This large excess suggests that the trapped-melt mechanism is more than sufficient to supply the BSM HSE budget, even if only a small fraction (~0.02–0.5%) of the deep solid mantle reservoir hosting trapped melt was eventually mixed into the convecting mantle through entrainment over geological time.

Independent evidence indicates that the Martian deep mantle was never fully homogenized, with large-scale chemical heterogeneities persisting since early differentiation (Cheng et al., 2024). Under such incomplete mixing, trapped metallic melt pockets could likewise have been preserved over billion-year timescales. The combination of initial melt trapping governed by the dihedral angle barrier demonstrated in this study (Figs. 6a-6b), and subsequent incomplete convective mixing (Fig. 6c), therefore provides a physically self-consistent explanation for

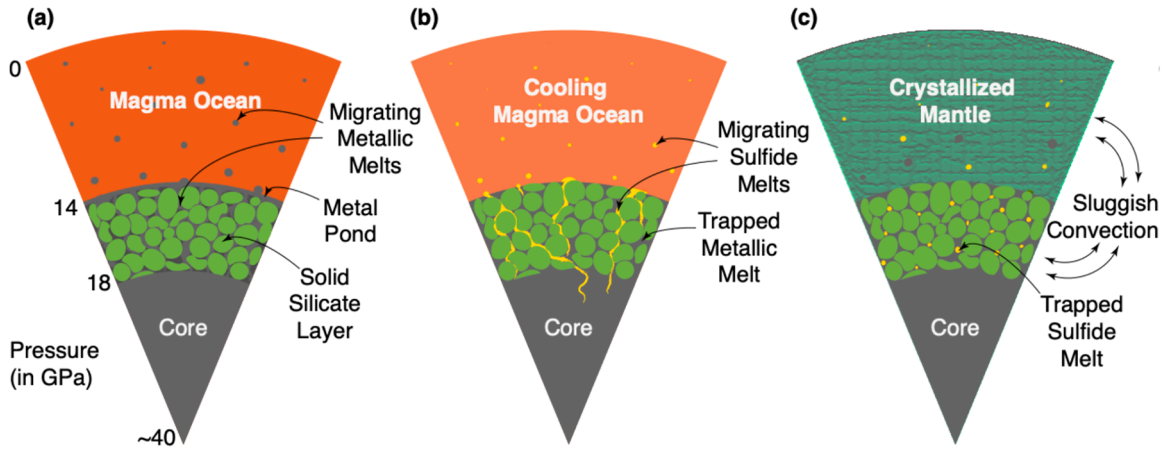

Fig. 6. Schematic illustration of the segregation, ponding, percolation, and trapping of metallic and sulfide melts in the Martian mantle. **(a)** Metallic melt segregates from the magma ocean, sinks, and ponds at its base (Metal Pond), equilibrating with HSEs in the surrounding silicate melt. Metal that remains dispersed at the grain scale migrates via percolation along grain edges in the solid silicate layer. **(b)** Because the dihedral angle of the metallic melt exceeds the critical angle of 60°, percolation requires the melt fraction to exceed a critical threshold; melt that fails to reach this threshold, or that becomes stranded upon drainage, is trapped within the solid silicate layer as a residual melt fraction (Trapped Metallic Melt). Simultaneously, sulfur that exceeded sulfide contents at sulfide saturation (SCSS) in the magma ocean exsolves as sulfide melt and segregates downward (the "Hadean matte"). The sulfide melt equilibrates with HSEs in the magma ocean before percolating into the underlying solid silicate layer (Migrating Sulfide Melts). **(c)** Because the dihedral angle of the sulfide melt also exceeds 60°, melt connectivity is limited, and part of the melt becomes trapped as isolated pockets within the solid mantle (Trapped Sulfide Melt). If mantle convection is sluggish, only a small portion of the solid silicate layer containing trapped melts may be incorporated into the convecting mantle over geological timescales (Sluggish Convection). Symbol sizes are not to scale and do not represent actual melt volumes.

the HSE abundances observed in BSM without requiring late veneer, although a late veneer contribution is not precluded (Walker, 2009; Wang and Becker, 2017). For this scenario to be consistent with the positive correlation between siderophile and lithophile incompatible elements (e.g., Mo-Ce, W-La, P-Ti) observed in the Martian basaltic meteorites (Righter and Chabot, 2011; Righter et al., 1998), entrained metal would be oxidized and incorporated into the silicate mantle prior to any subsequent melting event. The small fraction required (~0.02–0.5%) may make complete oxidation over geological timescales more plausible, but the detailed mechanism has not been demonstrated and remains an open question for future work.

Beyond HSEs, trapped metallic melts would also sequester siderophile volatile elements, specifically carbon and nitrogen. Under the moderately reducing conditions of Martian differentiation ($\Delta IW \sim -1.5$ to -0.5), both carbon and nitrogen partition strongly into metallic and sulfide melts (Grewal et al., 2021a, 2019a, 2021b; Grewal et al., 2019b; Tsuno et al., 2018). Retention of even a small fraction of metallic melt in the solid mantle would therefore sequester a substantial share of the mantle's C and N, which may contribute to the apparent depletion of these volatiles in the Martian mantle relative to chondritic sources.

5. Conclusion

We report the first experimental determination of dihedral angles between Fe(-Ni)-S-O alloy melts and majorite garnet at conditions relevant to the deep Martian mantle (18 GPa, 1723–2200 K), alongside new measurements in the ringwoodite system. Our principal findings are:

(1) Dihedral angles decrease systematically with increasing temperature, total S + O content, and fO_2, whereas Ni has no measurable effect. These dependencies are consistent with the known surface-active behavior of S and O in metallic melts and the role of FeO in reducing solid-melt interfacial energy.
(2) Under comparable conditions, dihedral angles in majorite garnet are consistently ~10° lower than in ringwoodite, the first experimental evidence that the host mineral phase influences the wetting behavior of metallic melts at transition-zone pressures. This difference likely reflects the multi-component chemical nature of majorite, which may lower the solid-melt interfacial energy relative to the structurally simpler ringwoodite.
(3) Despite this reduction, all measured dihedral angles remain well above 60° (89°–126°), demonstrating that the entire mineral assemblage at ~18 GPa, both ringwoodite and majorite garnet, constitutes a percolation barrier for metallic melts. Because our experimental compositions are more S-rich than the primary core-forming alloy (~15 mol% S), the measured values represent lower bounds; the barrier for core-forming metal was even more severe.
(4) Equilibrium metal-silicate and sulfide-silicate partitioning predicts HSE concentrations in the Martian mantle that are ~50–12,000 times lower than observed BSM values. Even a conservatively estimated trapped melt fraction of ~2 vol.% produces an HSE reservoir ~200–4500 × larger than BSM, demonstrating that the percolation barrier identified in this study provides a quantitatively viable mechanism for HSE retention, and potentially for siderophile volatiles such as C and N, without requiring a late veneer.

These results demonstrate that the completeness of metal-silicate separation in terrestrial planets depends not only on the dynamics of the magma ocean itself, but also on the percolation properties of the underlying solid mantle – specifically the dihedral angles imposed by its constituent mineral phases. This mineralogical control on differentiation efficiency has been overlooked in previous models and may be relevant to other differentiated bodies where transition-zone phases were stable during core formation.

CRediT authorship contribution statement

Kyusei Tsuno: Conceptualization, Funding acquisition, Investigation, Methodology, Project administration, Visualization, Writing – original draft, Writing – review & editing. **Hideharu Kuwahara:** Investigation, Methodology, Writing – review & editing. **Varun Manilal:** Investigation, Writing – review & editing. **Axel Wittmann:** Writing – review & editing. **Kurt Leinenweber:** Methodology. **Tetsuo Irifune:**

Methodology. **Damanveer S Grewal:** Conceptualization, Funding acquisition, Methodology, Project administration, Supervision, Writing – original draft, Writing – review & editing.

Declaration of competing interest

The authors declare that they have no other known competing financial interests or personal relationships that could have appeared to influence the work reported in this paper.

Acknowledgement

A.P. Vyas created the final version of the schematic diagram in Fig. 6. We thank two anonymous reviewers for their constructive comments. This study was supported by start-up funds by Yale University to D.S.G. We acknowledge the use of facilities through the PRIUS program at the Geodynamics Research Center (GRC), Ehime University, as well as the Eyring Materials Center and the Facility for Open Research in a Compressed Environment (FORCE) (supported by the National Science Foundation under Mid-scale Research Infrastructure-1 Grant 2131833; PI: K.L.) at Arizona State University.

Supplementary materials

Supplementary material associated with this article can be found, in the online version, at doi:10.1016/j.epsl.2026.120246.

Data availability

All data supporting this study, including dihedral angle measurements and mineral compositions, have been included as part of the Supplementary file.

References

Ballhaus, C., Ellis, D.J., 1996. Mobility of core melts during Earth's accretion. Earth. Planet. Sci. Lett. 143, 137–145.
Bertka, C.M., Fei, Y., 1997. Mineralogy of the Martian interior up to core-mantle boundary pressures. J. Geophys. Res. 102, 5251–5264.
Blanchard, I., Abeykoon, S., Frost, D.J., Rubie, D.C., 2021. Sulfur content at sulfide saturation of peridotitic melt at upper mantle conditions. Am. Mineral. J. Earth Planet. Mater. 106, 1835–1843.
Bouvier, L.C., Costa, M.M., Connelly, J.N., Jensen, N.K., Wielandt, D., Storey, M., Nemchin, A.A., Whitehouse, M.J., Snape, J.F., Bellucci, J.J., 2018. Evidence for extremely rapid magma ocean crystallization and crust formation on Mars. Nature 558, 586–589.
Chakraborty, S., 2010. Diffusion coefficients in Olivine, Wadsleyite and Ringwoodite. Rev. Mineral. Geochem. 72, 603–639.
Cheng, K.W., Rozel, A.B., Golabek, G.J., Ballantyne, H.A., Jutzi, M., Tackley, P.J., 2024. Mars's crustal and volcanic structure explained by southern giant impact and resulting mantle depletion. Geophys. Res. Lett. 51, e2023GL105910.
Dreibus, G., Palme, H., 1996. Cosmochemical constraints on the sulfur content in the Earth's core. Geochim. Cosmochim. Acta 60, 1125–1130.
Dreibus, G., Wanke, H., 1985. Mars, a volatile-rich planet. Meteoritics (ISSN 0026-1114), vol. 20, pt. 2, June 30, 1985, p. 367–381. DFG-supported research. 20, 367–381.
Duncan, M.S., Schmerr, N.C., Bertka, C.M., Fei, Y., 2018. Extending the solidus for a model iron-rich Martian mantle composition to 25 GPa. Geophys. Res. Lett. 45 (10), 220, 211–210.
Fleck, J., Rains, C., Weeraratne, D., Nguyen, C., Brand, D., Klein, S., McGehee, J., Rincon, J., Martinez, C., Olson, P., 2018. Iron diapirs entrain silicates to the core and initiate thermochemical plumes. Nat. Commun. 9, 71.
Frost, D.J., 2003. Fe2+-Mg partitioning between garnet, magnesiowustite, and (Mg, Fe) 2SiO4 phases of the transition zone. Am. Mineral. 88, 387–397.
Gaetani, G.A., Grove, T.L., 1999. Wetting of mantle olivine by sulfide melt: implications for re/Os ratios in mantle peridotite and late-stage core formation. Earth Planet. Sci. Lett. 169, 147–163.
Ghanbarzadeh, S., Hesse, M.A., Prodanović, M., 2017. Percolative core formation in planetesimals enabled by hysteresis in metal connectivity. Proc. Natl. Acad. Sci. U.S. A. 114, 13406–13411.
Grewal, D.S., Dasgupta, R., Aithala, S., 2021a. The effect of carbon concentration on its core-mantle partitioning behavior in inner Solar System rocky bodies. Earth. Planet. Sci. Lett. 571, 117090.
Grewal, D.S., Dasgupta, R., Holmes, A.K., Costin, G., Li, Y., Tsuno, K., 2019a. The fate of nitrogen during core-mantle separation on Earth. Geochim. Cosmochim. Acta 251, 87–115.
Grewal, D.S., Dasgupta, R., Hough, T., Farnell, A., 2021b. Rates of protoplanetary accretion and differentiation set nitrogen budget of rocky planets. Nat. Geosci. 14, 369–376.
Grewal, D.S., Dasgupta, R., Sun, C., Tsuno, K., Costin, G., 2019b. Delivery of carbon, nitrogen, and sulfur to the silicate Earth by a giant impact. Sci. Adv. 5 eaau3669.
Groebner, N., Kohlstedt, D.L., 2006. Deformation-induced metal melt networks in silicates: implications for core–mantle interactions in planetary bodies. Earth. Planet. Sci. Lett. 245, 571–580.
Holzheid, A., Schmitz, M.D., Grove, T.L., 2000. Textural equilibria of iron sulfide liquids in partly molten silicate aggregates and their relevance to core formation scenarios. J. Geophys. Res. 105, 13555–13567.
Horan, M., Walker, R., Morgan, J., Grossman, J., Rubin, A., 2003. Highly siderophile elements in chondrites. Chem. Geol. 196, 27–42.
Huang, Q., Schmerr, N.C., King, S.D., Kim, D., Rivoldini, A., Plesa, A.C., Samuel, H., Maguire, R.R., Karakostas, F., Lekić, V., 2022. Seismic detection of a deep mantle discontinuity within Mars by InSight. Proc. Natl. Acad. Sci. U.S.A. 119, e2204474119.
Irving, J.C., Lekić, V., Durán, C., Drilleau, M., Kim, D., Rivoldini, A., Khan, A., Samuel, H., Antonangeli, D., Banerdt, W.B., 2023. First observations of core-transiting seismic phases on Mars. Proc. Natl. Acad. Sci. U.S.A. 120, e2217090120.
Jurewicz, S.R., Jurewicz, A.J., 1986. Distribution of apparent angles on random sections with emphasis on dihedral angle measurements. J. Geophys. Res. 91, 9277–9282.
Karner, J., Papike, J., Sutton, S., Shearer, C., McKay, G., Le, L., Burger, P., 2007. Valence state partitioning of Cr between pyroxene-melt: effects of pyroxene and melt composition and direct determination of Cr valence states by XANES. Application to martian basalt QUE 94201 composition. Am. Mineral. 92, 2002–2005.
Khan, A., Huang, D., Durán, C., Sossi, P.A., Giardini, D., Murakami, M., 2023. Evidence for a liquid silicate layer atop the Martian core. Nature 622, 718–723.
Khan, A., Sossi, P.A., Liebske, C., Rivoldini, A., Giardini, D., 2022. Geophysical and cosmochemical evidence for a volatile-rich Mars. Earth. Planet. Sci. Lett. 578, 117330.
Kruijer, T.S., Kleine, T., Borg, L.E., Brennecka, G.A., Irving, A.J., Bischoff, A., Agee, C.B., 2017. The early differentiation of Mars inferred from Hf–W chronometry. Earth. Planet. Sci. Lett. 474, 345–354.
Laurenz, V., Rubie, D.C., Frost, D.J., Vogel, A.K., 2016. The importance of sulfur for the behavior of highly-siderophile elements during Earth's differentiation. Geochim. Cosmochim. Acta 194, 123–138.
Manilal, V., Tsuno, K., Kuwahara, H., Wittmann, A., Pommier, A., Till, C., Grewal, D.S., 2026. Percolative core formation in oxidized planetesimals–I: experiments on melt migration in olivine aggregates. Geochim. Cosmochim. Acta in press.
Mann, U., Frost, D.J., Rubie, D.C., 2009. Evidence for high-pressure core-mantle differentiation from the metal–silicate partitioning of lithophile and weakly-siderophile elements. Geochim. Cosmochim. Acta 73, 7360–7386.
Minarik, W.G., Ryerson, F.J., Watson, E.B., 1996. Textural entrapment of core-forming melts. Science (1979) 272, 530–533.
Miura, T., Terasaki, H., Takaki, H., Kobayashi, K., Bromiley, G.D., Yoshino, T., 2025. The effect of pressure on dihedral angle between liquid Fe-S and orthopyroxene: implication for percolative core formation in planetesimals and planetary embryos. Meteorit. Planet. Sci. 60, 2811–2827.
Nishihara, Y., Takahashi, E., 2001. Phase relation and physical properties of an Al-depleted komatiite to 23 GPa. Earth. Planet. Sci. Lett. 190, 65–77.
O'Neill, H.S.C., 1991. The origin of the Moon and the early history of the Earth—A chemical model. Part 2: the Earth. Geochim. Cosmochim. Acta 55, 1159–1172.
Rai, N., Van Westrenen, W., 2013. Core-mantle differentiation in Mars. J. Geophys. Res. 118, 1195–1203.
Righter, K., 2025. The influence of ALH 84001 on our understanding of the origin and evolution of Mars. Meteorit. Planet. Sci. 60, 74–102.
Righter, K., Hervig, R., Kring, D., 1998. Accretion and core formation on Mars: molybdenum contents of melt inclusion glasses in three SNC meteorites. Geochim. Cosmochim. Acta 62, 2167–2177.
Righter, K., Chabot, N.L., 2011. Moderately and slightly siderophile element constraints on the depth and extent of melting in early Mars. Meteorit. Planet. Sci. 46, 157–176.
Rose, L.A., Brenan, J.M., 2001. Wetting properties of Fe-Ni-Co-Cu-OS melts against olivine: implications for sulfide melt mobility. Econ. Geol. 96, 145–157.
Rubie, D.C., Laurenz, V., Jacobson, S.A., Morbidelli, A., Palme, H., Vogel, A.K., Frost, D. J., 2016. Highly siderophile elements were stripped from Earth's mantle by iron sulfide segregation. Science (1979) 353, 1141–1144.
Rubie, D.C., Jacobson, S.A., 2016. Mechanisms and geochemical models of core formation. Deep Earth: Physics and Chemistry of the Lower Mantle and Core, pp. 181–190.
Samuel, H., Drilleau, M., Rivoldini, A., Xu, Z., Huang, Q., Garcia, R.F., Lekić, V., Irving, J. C., Badro, J., Lognonné, P.H., 2023. Geophysical evidence for an enriched molten silicate layer above Mars's core. Nature 622, 712–717.
Shannon, M., Agee, C., 1996. High pressure constraints on percolative core formation. Geophys. Res. Lett. 23, 2717–2720.
Shannon, M., Agee, C., 1998. Percolation of core melts at lower mantle conditions. Science (1979) 280, 1059–1061.
Steenstra, E., Lord, O., Vitale, S., Bullock, E., Klemme, S., Walter, M., 2022. Sulfur solubility in a deep magma ocean and implications for the deep sulfur cycle. Geochem. Perspect. Lett. 22, 5–9.
Stevenson, D., 1990. Core Formation ed H. Newsom and JE Jones. Oxford Univ. Press, Oxford.
Stähler, S.C., Khan, A., Banerdt, W.B., Lognonné, P., Giardini, D., Ceylan, S., Drilleau, M., Duran, A.C., Garcia, R.F., Huang, Q., 2021. Seismic detection of the martian core. Science (1979) 373, 443–448.

Tang, H., Dauphas, N., 2014. 60Fe–60Ni chronology of core formation in Mars. Earth. Planet. Sci. Lett. 390, 264–274.
Taylor, G.J., 2013. The bulk composition of Mars. Geochemistry 73, 401–420.
Terasaki, H., Frost, D.J., Rubie, D.C., Langenhorst, F., 2005. The effect of oxygen and sulphur on the dihedral angle between Fe–O–S melt and silicate minerals at high pressure: implications for Martian core formation. Earth. Planet. Sci. Lett. 232, 379–392.
Terasaki, H., Frost, D.J., Rubie, D.C., Langenhorst, F., 2007. Interconnectivity of Fe–O–S liquid in polycrystalline silicate perovskite at lower mantle conditions. Phys. Earth Planet. Inter. 161, 170–176.
Terasaki, H., Frost, D.J., Rubie, D.C., Langenhorst, F., 2008. Percolative core formation in planetesimals. Earth. Planet. Sci. Lett. 273, 132–137.
Terasaki, H., Urakawa, S., Funakoshi, K., Nishiyama, N., Wang, Y., Nishida, K., Sakamaki, T., Suzuki, A., Ohtani, E., 2009. In situ measurement of interfacial tension of Fe–S and Fe–P liquids under high pressure using X-ray radiography and tomography techniques. Phys. Earth Planet. Inter. 174, 220–226.
Tonks, W.B., Melosh, H.J., 1993. Magma ocean formation due to giant impacts. J. Geophys. Res. 98, 5319–5333.
Tsuno, K., Grewal, D.S., Dasgupta, R., 2018. Core-mantle fractionation of carbon in Earth and Mars: the effects of sulfur. Geochim. Cosmochim. Acta 238, 477–495.
Tsuno, K., Grewal, D.S., Xu, V., Leinbach, L., Leinenweber, K., Wittmann, A., Shim, S.H., 2024. The effect of nitrogen on the dihedral angle between Fe− Ni melt and ringwoodite: implications for the nitrogen deficit in the bulk silicate earth. Geophys. Res. Lett. 51, e2024GL109584.
van Mierlo, W.L., Langenhorst, F., Frost, D.J., Rubie, D.C., 2013. Stagnation of subducting slabs in the transition zone due to slow diffusion in majoritic garnet. Nat. Geosci. 6, 400–403.
von Bargen, N., Waff, H.S., 1986. Permeabilities, interfacial areas and curvatures of partially molten systems: results of numerical computations of equilibrium microstructures. J. Geophys. Res. 91, 9261–9276.
Walker, R.J., 2009. Highly siderophile elements in the Earth, Moon and Mars: update and implications for planetary accretion and differentiation. Geochemistry 69, 101–125.
Walte, N., Rubie, D., Bons, P., Frost, D., 2011. Deformation of a crystalline aggregate with a small percentage of high-dihedral-angle liquid: implications for core–mantle differentiation during planetary formation. Earth. Planet. Sci. Lett. 305, 124–134.
Wang, Z., Becker, H., 2017. Chalcophile elements in Martian meteorites indicate low sulfur content in the Martian interior and a volatile element-depleted late veneer. Earth. Planet. Sci. Lett. 463, 56–68.
Wang, L., Fei, Y., 2023. A partially equilibrated initial mantle and core indicated by stress-induced percolative core formation through a bridgmanite matrix. Sci. Adv. 9 eade3010.
Yoshizaki, T., McDonough, W.F., 2020. The composition of Mars. Geochim. Cosmochim. Acta 273, 137–162.
ZhangZhou, J., Li, Y., Chowdhury, P., Sen, S., Ghosh, U., Xu, Z., Liu, J., Wang, Z., Day, J. M., 2024. Predicting sulfide precipitation in magma oceans on Earth, Mars and the Moon using machine learning. Geochim. Cosmochim. Acta 366, 237–249.